Biophysical Journal, Volume *112*

Supplemental Information

New Continuum Approaches for Determining Protein-Induced Membrane Deformations

David Argudo, Neville P. Bethel, Frank V. Marcoline, Charles W. Wolgemuth, and Michael Grabe

Supporting Material: New continuum approaches for determining protein induced membrane deformations

David Argudo*, Neville P. Bethel*, Frank V. Marcoline*, Charles W. Wolgemuth‡ and Michael Grabe*

* *Cardiovascular Research Institute, Department of Pharmaceutical Chemistry, University of California San Francisco, San Francisco, CA 94158, USA.*

‡ *Departments of Molecular and Cellular Biology and Physics, University of Arizona, Tucson, Arizona.*

S1. Analysis of molecular dynamics membrane deformation profiles: effects at the boundaries

To compare molecular dynamics (MD) simulation results with our continuum-atomistic model, we averaged lipid positions of individual MD snapshots to obtain a final equilibrium membrane shape. The procedure is described in *Simulation Methods* in the main text. Fig. S1 shows the running time average of the membrane thickness, which indicates the time required to average out spatial fluctuations to arrive at a converged static pattern. Panel (A) contains a gramicidin dimer and (B) is a protein free bilayer. Analysis of these profiles reveals several interesting features. First, even at 100 ns, the protein free system exhibits a spatial pattern showing inhomogeneity present in the starting configuration. The magnitude of the inhomogeneity is much reduced (10 Å at 25 ns versus 4 Å at 100 ns), and it is centered on the bulk equilibrium thickness of 28.5 Å, but a pattern persists nonetheless. The pinching pattern in the gramicidin simulations is set up quickly (in 25 ns), but the spatial fluctuations are so large that the system must be averaged for at least 250 ns before a somewhat static pattern emerges. This time difference when compared to the protein-free system is not surprising since the membranes are pre-equilibrated in a flat undeformed state closer to the protein-free simulation. But we want to point out that even these simple simulations must be averaged for 200 ns, preferably more (500 ns in the main text), to achieve static patterns. Second, protein induced deformations extend to the simulation boundaries indicating that bilayer patch size should be carefully considered to allow full relaxation to bulk values at the boundaries. At 250 ns, panel (A) shows the membrane height reaches bulk values (28.5 Å) at the corners of the periodic box (55 Å from the center), but not at the centers of each side (40 Å from the center). If the box is too small, periodic boundary conditions will muddy interpretation of the patterns.

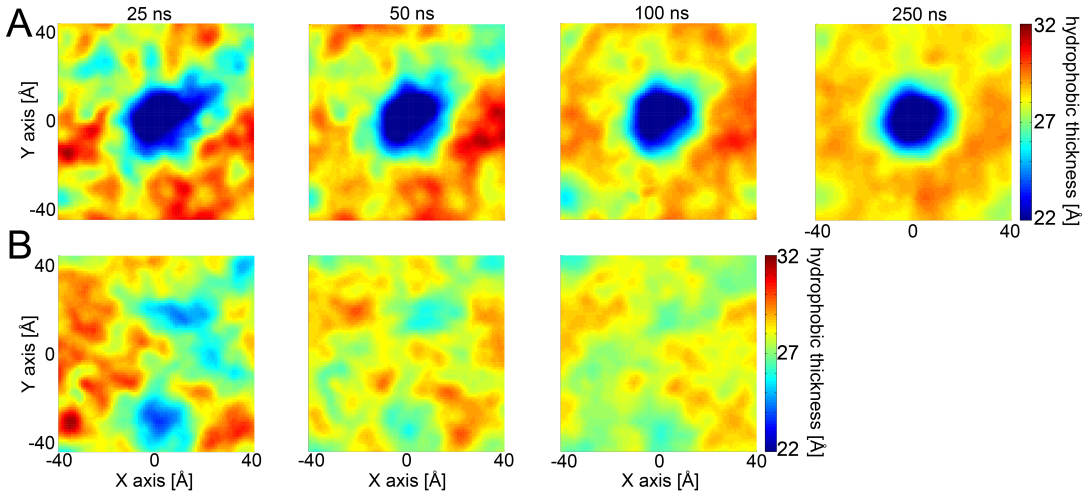

Figure S1: Running time average of hydrophobic mismatch from MD simulations with gramicidin (A) and without protein (B). Both systems contain POPC lipids. In panel A, membrane height values converge to the bulk value (~28.5 Å) at the corners of the simulation box between 100 ns and 250 ns, but the pattern is still fluctuating when averaged for less time. Moreover, at the center of the outer edges of the box (40 Å from the protein) the membrane heights are 2-3 Å higher than bulk values. (B) MD simulation of a pure POPC membrane. Even after averaging for 100 ns a spatial pattern persists, but the amplitude of the fluctuations is only ±2 Å from the mean value of 28.5 Å.

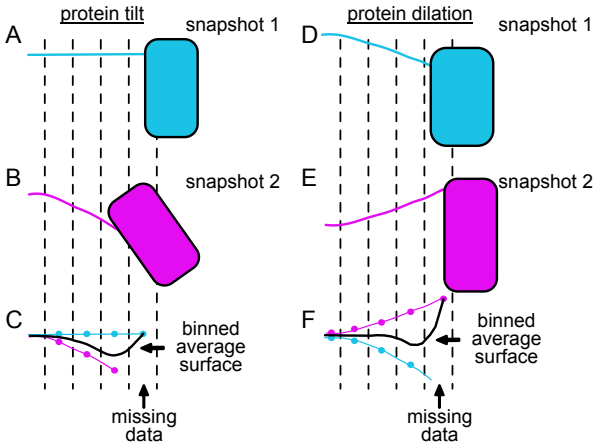

Figure S2: Averaging membrane configurations can produce unrealistic surfaces. (A-B) Binning a straight (A) and tilted (B) protein configuration. When the protein tilts to the left, the protein-membrane boundary also shifts to the left. (C) Combining bins from configurations A and B leads to non-monotonic behavior that is otherwise not present in either configuration. (D-E) Binning membrane surfaces from snapshots in which the protein radius is dilated (D) or constricted (E). The later configuration is representative of what occurs during the creation of *hotspots* in which individual lipid molecules extend over the top of the channel to interact with specific tryptophan residues. (F) Combining bins from configurations D and E leads to non-monotonic behavior, which is not representative of either configuration.

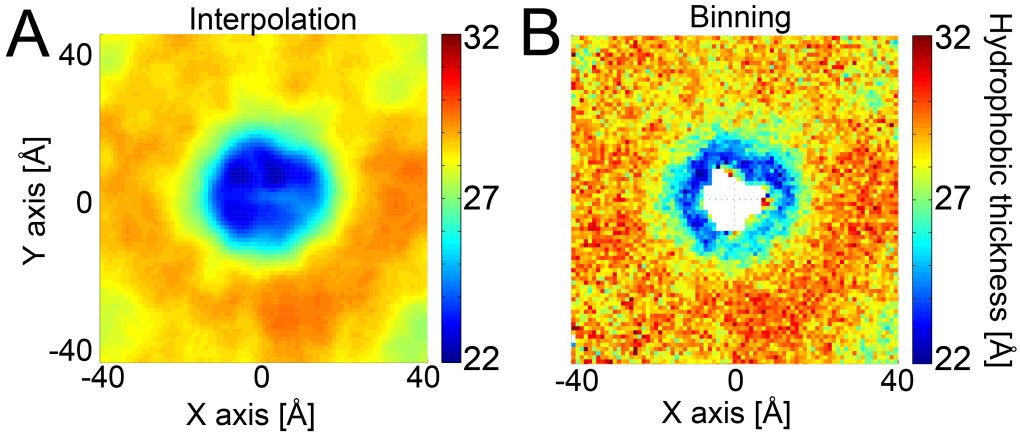

Figure S3: Different averaging methods produce different membrane hydrophobic thickness profiles. (A) Surface profile obtained using an interpolation averaging method. For each snapshot, membrane heights are first interpolate to a two dimensional grid of one Å spacing. All grid points are evaluated regardless of protein occupancy. The final surface is the average of all grids over the course of the trajectory. We see that extending radially away from the center of the membrane, the deformation profile exhibits pure monotonic behavior (blue to red) within a distance comparable to the width of a few lipid shells. (B) Surface profile obtained using a bin-based averaging method that simply averages local lipid height in each snapshot (each bin is 1 $Å^2$). Unlike the method in panel (A), if a lipid is not located within a bin for a given snapshot, the bin will receive no value. For bins near the protein boundary, they are often occupied by protein, and hence rarely populated by lipid. There are several localized *hotspots* adjacent to the protein where the membrane becomes very thick, 32 Å. Extending radially away from the protein in these regions, the membrane deformation profile exhibits non-monotonic behavior within a distance comparable to the width of a few lipid shells. The simulation system is composed of POPC lipids and the protein is gramacidin. For both methods, the protein was centered from snapshot to snapshot prior to computing membrane heights.

We carefully considered several methods for averaging the surfaces from MD, because the average of a solution set often results in an entity that is not a member of the set. However, averaged membrane surface profiles should reflect, as much as possible, an equilibrium membrane distortions that is physically allowable. Gramicidin is a small peptide and during MD simulations the protein position and tilt orientation fluctuate resulting in corresponding fluctuations in the protein-membrane boundary. If these changes are not carefully accounted for during averaging, it can magnify artifacts resulting from averaging. One option for averaging involves binning membrane height at the upper and lower leaflets to determine the thickness profile. To do this, we created a 2D grid of squares 1 Å in size, one for the upper surface and one for the lower surface, and recorded the heights of upper/lower lipid molecules in each respective bin for every snapshot. However, as shown in Fig S2 this approach leads to two scenarios that produce artifacts when binning results from MD. Panels (A-C) show the effect of binning straight (A) and tilted (B) protein configurations. Panel (C) shows how the tilted configuration in (B) results in missing data, and combining bins from configurations (A) and (B) leads to non-mononotic behavior that is otherwise not present in either true configuration. Similarly panels (D-F) show the effect of binning a protein with a dilated effective radius (D) at one point in time and constricted effective radius (B) at another. The averaged surface in (F) has missing data resulting from configuration (D), and it also exhibits non-monotonic behavior. This later scenario occurs during the creation of *hotspots* in which individual lipid molecules extend over the top of the channel to interact with specific tryptophan residues (1). When *hotspots* are present, the effective protein area is reduced due to lipids encroach on the protein-occupied region. Panel (F) shows how combining bins from both configurations leads to non-mononotic behavior that is otherwise not present in (D) or (E).

As an alternative approach to determining representative, averages of the membrane surface, we used an interpolation procedure where each node value of a Cartesian grid was assigned the interpolated z-value of nearby lipid C2 carbon atoms for each MD snapshot. This approach guarantees that every node of the surface has a value for each membrane configuration. Fig. S3 shows a comparison between the membrane thickness obtained using the interpolation (A) and binning (B) methods. In the interpolation averaging procedure (A) the membrane deformation profile that extends radially away from the protein exhibits a monotonic behavior (blue to red) within a distance comparable to the width of a few lipid shells, while the binning method (B) generates a non-monotonic radial profile arising from *hotspots* near the protein (red and yellow) with increased thickness. Analysis of the specific MD snapshots that give rise to the non-monotonic behavior in the averaged surfaces in Fig. S3 B are themselves radially monotonic near the protein indicating that the averaged thickness profile harbors artifacts likely resulting from the mechanisms illustrated in Fig. S2. Moreover, the non-monotonic profile is highly curved with a high corresponding deformation energy casting further doubts on the physical appropriateness of the binning scheme. A deeper analysis of the influence *hotspots* (black or white circled region) play on the binned hydrophobic profile (reproduced in Fig. S4 A) shows that they are poorly sampled bins (panel B), yet they dramatically influence the final average thickness. We computed the membrane thickness with this sparse data corresponding to only membrane configurations in which the textithotspot was populated, and the resulting average profile is radially monotonic within the first few lipid shells (panel (C)). Importantly, the membrane is quite thick for these snapshots, but the radial relaxation is smooth. We conclude that individual membrane configurations are quite smooth in the first few lipid shells adjacent to the protein, and simple binning schemes mask this observation.

S2. Non-Elastic Energy terms

S2.1. Electrostatic Energy $G^{(e)}$

The electrostatic energy of the inclusion in the bilayer was determined using the non-linear Poisson-Boltzmann equation (in e.s.u-c.g.s unit system) (2, 3):

$$-\nabla \cdot [\epsilon(\vec{p})\nabla\phi(\vec{p})] + \epsilon(\vec{p})\kappa^2(\vec{p})\sinh[\phi(\vec{p})] = \frac{e}{k_{\mathrm{B}}T}4\pi\rho(\vec{p}), \quad \phi(\vec{p}) = \frac{e\Phi(\vec{p})}{k_{\mathrm{B}}T}, \tag{S1}$$

where $\phi(\vec{p})$ is the reduced electrostatic potential at position $\vec{p}$, k_{B} is the Boltzmann constant, T is the absolute temperature, κ is the Debye-Huckel screening coefficient, ϵ is the spatially-dependent dielectric constant, ρ is the space-dependent charge density within the protein and e is the elementary charge. The electrostatic calculations were carried out using the APBS software (3) together with modifications to include membrane dielectric effects as described in

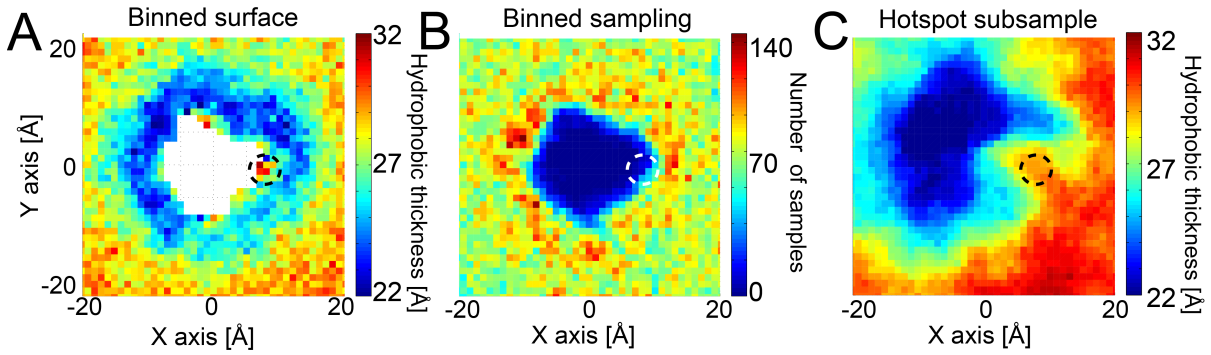

Figure S4: Hotspots are rare, but still smooth. (A) Binned POPC average thickness around gramicidin (same as Fig. S3 B). The dashed oval encompasses a single *hotspot* where lipids extend up over the channel, and the oval corresponds to the region in all three panels. (B) Bin occupancy by lipids during MD simulation. The *hotspot* is rarely sampled by a lipid. (C) Membrane thickness calculated using only snapshots in which a lipid occupies the *hotspot*. The surface was constructed with the interpolation method, since binning resulted in a highly discontinuous surface due to poor sampling. The resulting profile is monotonic and smooth in the radial direction, and these properties are present in the individual snapshots.

Callenberg (4). As in our recent work Ref. (5), a six way flood fill method is used to add the dielectric influence of the membrane to the protein system. Additional details on the electrostatic calculations can be found in our previous publications (5, 6). Finally, we point out that in our calculations we include the effects of ionic screening, but find that the strength of the ionic solution has little effect in the membrane deformations induced by gramicidin. Setting the ionic strength to zero or increasing it by an order of magnitude changes the energy by less than 0.5 kcal/mol.

S2.2. Nonpolar Energy $G^{(np)}$

The non-polar energy of the protein in the membrane environment is related to the amount of protein surface area buried in the membrane. Here, we assume the non-polar energy is:

$$G^{(np)} = a \cdot (A_{mem} - A_{sol}) \,, \tag{S2}$$

where A_{mem} is the protein's solvent accessible surface area (SASA) in the membrane and A_{sol} is the total SASA in solution. The total protein A_{sol} and per atom surface areas are calculated using Michael Sanner's Molecular Surface program, MSMS (7). To determine A_{men}, membrane exposed atoms were first identified using the same six way flood fill algorithm used for the electrostatic calculations. Atoms that are determined to be membrane exposed are set to have an $A_{mem} = 0.0$. The nonpolar energy of each atom was calculated based on its height relative to the leaflets of the membrane. For atoms in the membrane core, its SASA was multiplied by the surface tension, $a = 0.028$ (kcal/mol)/Å^2. For atoms in the headgroup regions, the surface tension constant decays linearly from 0.028 to 0.00 (kcal/mol)/Å^2 over the 8 Å thickness of the headgroups. The phenomenological constant 0.028 (kcal/mol)/Å^2 is taken from the work of Sitkoff and co-workers (8), and we ignore the constant term usually found in these treatments to zero given that it is typically a small energetic value when compared to other terms in our theory. For more details see Refs. (5, 6).

S2.3. Protein Orientational Entropy $G^{(o)}$

The orientational entropy cost is the energetic penalty associated with the protein's inability to explore certain configurations when inserted in the membrane, which can be expressed in terms of the Euler angles ρ, θ and ϕ describing the protein's orientation in the membrane. The angle ρ represent rotations about the long axis of the protein, θ is the angle created between the z-axis of the membrane and the long axis of the protein (See Fig. 3 in main text), and ϕ represents rotations of the protein about the z-axis of the membrane. As the protein axis tips away from the membrane normal (θ), it is able to explore a greater number of states associated with free rotation about ϕ. The entropy at a given θ value in the range $\delta\theta$ is related to the area swept out by the tip of the protein as it rotates about ϕ. Thus, the entropic

energy change with respect to the protein aligned with the membrane normal is given by:

$$G^{(o)} = -k_B T \ln\left(\frac{\Delta A_\theta}{\Delta A_0}\right), \tag{S3}$$

where ΔA_θ is the area swept out by the tip of the helix over the surface of a sphere and ΔA_0 is the effective area explored by the helix tip when it is oriented vertically. The ratio in areas is then given by:

$$\frac{\Delta A_\theta}{\Delta A_0} = \frac{\int_{\theta-\delta\theta}^{\theta+\delta\theta} \sin\theta d\theta}{\int_0^{\delta\theta} \sin\theta d\theta}, \tag{S4}$$

where $\delta\theta \approx r/h$ accounts for tilt angle spanned by a cylinder of finite radius r and height h.

S3. Geometrical description of the membrane

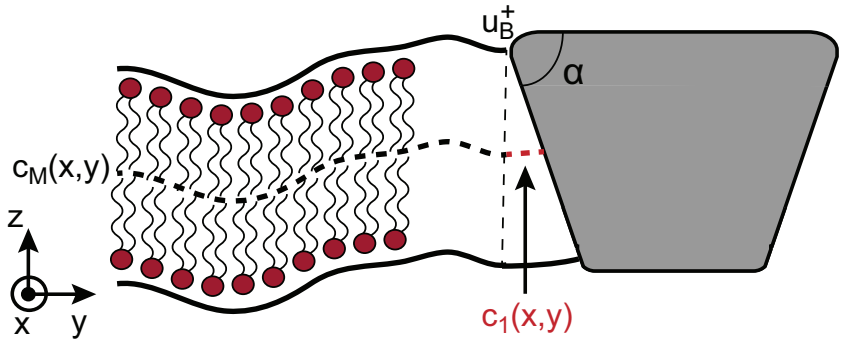

Figure S5: Cartoon model of the membrane in the presence of a conically shaped protein. In the regions where the upper and lower leaflet both exist, the compression surface is labeled $c_M(x, y)$, while in regions where either the upper or lower leaflet does not exist, the compression surface is labeled $c_1(x, y)$. The variable u_B^+ corresponds to the membrane boundary displacements at the interface between the protein and the upper leaflet. The angle α of the conically shaped protein can be used to describe the degree of mismatch between the upper and lower leaflets.

We start by defining the geometry of the system. In Fig. S5, we illustrate a special case where the conical shape of an inclusion causes a mismatch between a region of the upper monolayer and the lower monolayer. A lack of corresponding patch along the z-direction poses a problem for the compression coupling between the leaflets. In general, protein shapes are complex, and this coupling problem arises in many instances. To address this type of biological problems we propose a two-sheet membrane model where the compression of each sheet is derived independently with respect to the bilayer compression surface $c_M(x, y)$ which acts as the coupling element between leaflets (Fig. S5).

We use small deflection theory (9, 10) to model the monolayer surfaces. We define the normal vector to the surface representing the upper monolayer as $\vec{N}^+$ and the lower monolayer as $\vec{N}^-$, which are approximately given by the following relations (9, 11):

$$\vec{N}^+ = \left\{\frac{\partial h^+}{\partial x_1}, \frac{\partial h^+}{\partial x_2}, -1\right\}, \quad \vec{N}^- = -\left\{\frac{\partial h^-}{\partial x_1}, \frac{\partial h^-}{\partial x_2}, -1\right\}. \tag{S5}$$

The variables $h^\pm(x_1, x_2)$ represent the shape, or distance from $z = 0$, of each leaflet. From the shape variables, we define the normalized variables $u^\pm(x_1, x_2)$ as the difference between the shape function of the upper and lower monolayer $h^\pm(x_1, x_2)$ with respect to the flat, undistorted monolayer thickness h_0:

$$u^\pm(x_1, x_2) = h^\pm(x_1, x_2) \mp h_0. \tag{S6}$$

The deformation represented by the leaflet shape variables given in Eq. S6 is equivalent to the mathematical description of bilayer deformation in terms of a dilation variable $d = (u^+ - u^-)/2$ and the bilayer midplane $h = (u^+ + u^-)/2$ (12). Finally, it important to distinguish the true monolayer surface in three dimensional space ($\Gamma^\pm$) from the two dimensional projection of the surface used in calculations ($\Omega^\pm$):

$$d\Gamma^\pm \approx \left[\sqrt{1 + (\nabla u^\pm)^2}\right] d\Omega^\pm \approx \left[1 + \frac{(\nabla u^\pm)^2}{2}\right] dxdy, \tag{S7}$$

where $d\Omega^\pm$ is the differential $dxdy$ in the projected plane (9).

S4. Elastic energy of an arbitrarily shaped inclusion in the membrane

We describe the total elastic energy of the system as the sum of the independent contributions of each monolayer:

$$G^T = E_m^+ + E_m^-, \tag{S8}$$

where +/− denotes variable associated with the upper/lower monolayer, respectively. We account for energies associated with mean curvature bending ($E_B^\pm$), changes in the area per lipid (compression) ($E_C^\pm$), surface tension ($E_S^\pm$), and changes in the gaussian curvature ($E_G^\pm$):

$$E_m^\pm = E_B^\pm + E_S^\pm + E_C^\pm + E_G^\pm, \tag{S9}$$

where each term is briefly described in the following sections.

S4.1. Mean bending curvature

The bending energy is (9):

$$E_B^\pm = \frac{1}{2}\int_{\Gamma^\pm} K_b^\pm \left(2H^\pm + J_0^\pm\right)^2 d\Gamma^\pm, \tag{S10}$$

where the integration is performed over each monoloyer surface $\Gamma^\pm$, $K_b^\pm$ are the monolayer bending moduli, $H^\pm$ are the mean curvature fields describing the neutral surfaces of each monolayer, and $J_0^\pm$ are the spontaneous curvatures in each leaflet. Under small deformations, the mean curvature can be approximated as (9, 13):

$$H^+ = \vec{\nabla}\vec{N}^+ \approx \frac{1}{2}\nabla^2 u^+(x_1, x_2) \quad \text{and} \quad H^- = \vec{\nabla}\vec{N}^- \approx -\frac{1}{2}\nabla^2 u^-(x_1, x_2). \tag{S11}$$

For the chosen normal vectors in Eq. S5 positive curvature H^+ at the upper leaflet is a concave up shape, while positive curvature H^- at the lower leaflet is concave down. The plus sign in front of the spontaneous curvature term $J_0^\pm$ follows the standard convention that a lipid in equilibrium with a positive spontaneous curvature is one with a large headgroup that prefers to adopt a micelle geometry (9). Since this sign convention varies in the literature, care must be taken when comparing different Hamiltonians (9, 10).

Making use of the definitions of the projected area and expanding up to quadratic order in the deformation variables, the bending energy is (9):

$$E_B^\pm \approx \frac{1}{2}\int_{\Omega^\pm} K_b^\pm \left(\nabla^2 u^\pm \pm J_0^\pm\right)^2 + \frac{K_b^\pm}{2}\left(J_0^\pm\right)^2 (\nabla u^\pm)^2 \, dxdy. \tag{S12}$$

S4.2. Surface tension

The tension/stretching energy ($E_S^\pm$) for each monolayer can be written as (9):

$$E_S^\pm = \int_{\Gamma^\pm} \sigma^\pm d\Gamma^\pm - \sigma^\pm \Gamma_0, \tag{S13}$$

where σ is the surface tension parameter, and the integration is performed along the neutral surface of each monoloyer $\Gamma^\pm$. Γ_0 is the initial undeformed area of the membrane, and it is the same for both upper and lower monolayers. Making use of Eq. S7, we can rewrite expression Eq. S13 as:

$$E_S^\pm = \frac{1}{2}\int_{\Omega^\pm} \sigma^\pm (\nabla u^\pm)^2 \, dxdy. \tag{S14}$$

It is important to point out that the surface tension parameter σ is a subtle term that has generated significant controversy depending on its physical interpretation (9). For a detailed description of the numerous interpretations of this term, we refer the reader to the works of Schmid (14), Diamant (15) and Watson et al. (16). Here, we interpret σ to be the conjugate variable that opposes the addition of new area to the total bilayer surface Γ. For constant area per lipid, Γ is proportional to the total number of lipids, and therefore, σ plays the role of the chemical potential. Combining the $\nabla^2 u^{\pm}$ term in Eq. S12 with Eq. S14, we obtain the effective surface tension parameter $\gamma^{\pm} = \sigma^{\pm} + K_B^{\pm}(J_0^{\pm})^2/2$. In the main text, we have expressed the energy in terms of the effective surface tension $\gamma^{\pm}$.

In addition to the gradient term, $\sigma\,(\nabla u^{\pm})^2$, in the Hamiltonian, it is often common to find a linear term in the literature, $\sigma\,(u^+ - u^-)$, that arises due to changes in lipid area for a volume incompressible membrane (16–18). This linear term results in systematic change in the equilibrium thickness of the membrane (16, 18):

$$L_0^* = L_0\left(1 - \frac{\sigma}{K_a}\right), \tag{S15}$$

where K_a is the bilayer compression modulus, L_0 is the membrane thickness of a tension-free membrane and L_0^* is the new equilibrium membrane thickness. Using Eq. S15, we can rewrite our deformation variables $u^{\pm}$ with respect to L_0^* rather than L_0. By doing this change of reference configuration, we recover the same Hamiltonian (without a linear term) in our deformation variables u^+ and u^-. Membrane vesicles are known to burst when the tension goes beyond a few mN/m, but exact values for the surface tension as a function of the membrane composition and protein are unknown. For this reason we have decided to use $\sigma \approx 3$ mN/m as originally postulated by H.W. Huang (13) and often employed in more recent works (6, 19–22). Adding the linear term and keeping $\sigma \approx 3$ mN/m results in a membrane thickness shift $L_0 - L_0^*$ of less than 1.4%.

S4.3. Bilayer compression

As derived in Refs. (17, 23), the compression energy for each monolayer is given by:

$$E_C^{\pm} \approx \int_{\Omega^{\pm}} \frac{K_a^{\pm}}{2}\left(\frac{A^{\pm} - A_0}{A_0}\right)^2 d\Omega^{\pm}, \tag{S16}$$

where A_0 is the initial area per lipid and $A^{\pm}$ is the deformed area per lipid. The compression modulus of each monolayer does not need to be the same, hence K_a^+ represents the modulus for the upper leaflet and K_a^- is the modulus for the lower leaflet. As discussed later, for a protein of arbitrary shape with unmatched leaflet regions, a framework where the upper and lower leaflets can have different compression moduli becomes important when including *shell hardening* effects through spatially dependent moduli (1, 24) (see section S4.4).

Returning to Eq. S16, the compression energy can be rewritten in terms of the shape variables $u^{\pm}$ since the change in area $(A^{\pm} - A_0)$ is related to the vertical compression along the z-axis by means of the lipid volume constraint (25):

$$V = \chi V_0, \quad V_0 = h_0 A_0, \quad V = (h^+ - c)A^+ = -(h^- - c)A^-, \tag{S17}$$

where V_0 is the initial volume of the lipids, V is the volume of the lipids in the deformed configuration (assumed to be the same for the upper and lower leaflets) and $c(x, y)$ is the compression surface (11, 16, 26, 27) (Fig S5). The parameter $\chi \in [0, 1]$ is a phenomenological term describing the degree of volume conservation of the lipids before and after deformation. It is well known that the lipid volume is nearly incompressible (17, 25). For this reason, we have constrained our analysis in the main text to the incompressible case of $\chi \approx 1$, but note that our methods can accommodate lipid compressibility through the phenomenological variable χ. For a compressible lipid mix, there would be a new term appearing in the energy functional that can be treated as a line tension (linear on the deformation variable $u^{\pm}$). Having a line tension term in the energy functional can be easily accounted for using a change of variables (28, 29), resulting in no change to the form of the equilibrium equations. Using Eq. S17, the energetic penalty for compression in Eq. S16 can approximated up to quadratic order on the shape variables to be:

$$E_C = \int_{\Omega^+} \frac{K_a^+}{2h_0^2}\left[u^+ - c\right]^2 d\Omega^+ + \int_{\Omega^-} \frac{K_a^-}{2h_0^2}\left[u^- - c\right]^2 d\Omega^-. \tag{S18}$$

S4.3.1. Bilayer compression: matched regions

When the upper and lower leaflets match ($\Omega^+ = \Omega^- = \Omega_M$) the energy in Eq. S18 reduces to:

$$E_C = \int_{\Omega_M} \frac{K_a^+}{2h_0^2}\left[u^+ - c\right]^2 + \frac{K_a^-}{2h_0^2}\left[u^- - c\right]^2 d\Omega_M. \tag{S19}$$

For the static case, the deformations associated with the compression surface $c(x, y)$ will equilibrate very fast, and consequently, we can minimize over $c(x, y)$ without loss of generality (26, 27). The solution yields:

$$c(x, y) = \frac{K_a^+ u^+ + K_a^- u^-}{K_a^+ + K_a^-}. \tag{S20}$$

Using Eq. S20, the bilayer compression energy of the bilayer can be rewritten as:

$$E_C = \int_{\Omega_M} \frac{K_{eff}}{2h_0^2}\left[u^+ - u^-\right]^2 dxdy, \quad K_{eff} = \frac{K_a^+ K_a^-}{(K_a^+ + K_a^-)}, \tag{S21}$$

where K_{eff} is analogous to the effective spring constant of two Hookean springs coupled in series. In the main text, we have labeled the compression surface in matched regions $c = c_M(x, y)$.

S4.3.2. Bilayer compression: unmatched regions

When the area of protein insertion in the upper and lower leaflets do not match there is a region in space Ω_1 where the shape variable u^+ is not defined and/or a region Ω_2 where the variable u^- is not defined. For such scenarios, we expect that the surface of compression $c(x, y)$ is a function of the geometry of the inserted protein, where the energy minimization with respect to $c(x, y)$ is subject to a spatial constraint. As an illustrative example, we consider the insertion of a conically shaped protein shown in Fig. S5. In the unmatched region Ω_1 in the lower leaflet, the compression energy is described by:

$$E_C^- = \int_{\Omega_1} \frac{2K_a^-}{L_0^2}\left[u^- - c(x, y)\right]^2 - \lambda\left(c(x, y) - c_1\right) dxdy, \tag{S22}$$

where λ is the conjugate Lagrange multiplier to the constraint in the compression surface $c(x, y)$. The function c_1 is unknown and probably the result of complex coupling between the geometry of the membrane protein and distortion of the lipids. Fig. S5 shows a mismatch region between upper and lower surfaces that is described by an angle α. For small values of $(\pi/2 - \alpha)$ (small mismatch region Ω_1), we expect that the bilayer midplane c_M (compression surface in the matched region Ω_M) is not to heavily distorted such that the compression surface $c_1(x, y)$ in Ω_1 can be approximated as:

$$c_1(x, y) = \frac{h_B^+ + h^-(x, y)}{2}, \tag{S23}$$

where $h_B^+ = u_B^+ + h_0$ is the set of boundary conditions between the upper leaflet and protein (Fig. S5). Although we have used a conically shaped protein for illustrative purposes, the approximation in Eq. S23 is valid for proteins of arbitrary shape as long as the mismatched regions are moderately small. Importantly, this approximation preserves continuity of the midplane function $c(x, y)$ over the entire space. We make the same approximation in the lower leaflet for $u^-(x, y)$ in the region Ω_2:

$$c_2(x, y) = \frac{h_B^- + h^+(x, y)}{2}, \tag{S24}$$

where $h_B^- = u_B^- - h_0$ is the set of boundary conditions between the lower leaflet and protein (figure not shown). Note the deflection values $h^+(x, y)$ and $h^-(x, y)$ can in general vary in space along the boundary of the protein. In that case the values of h_B^+ and h_B^- inside the regions Ω_1 and Ω_2 are calculated through an interpolation procedure. We emphasize that in our proposed elastic model h_B^+ and h_B^- are prescribed as fixed conditions used to compute the compression plane $c(x, y)$ on mismatched regions.

S4.4. Hardening effects near the protein

The decreased conformational freedom of lipids near the boundary of an inclusion leads to greater molecular packing and greater resistance to elastic deformations – an effect known as *hardening* (1, 24). Partenskii and Jordan (24) accounted for this effect by developing a membrane free energy model where the elastic moduli were higher at the boundary of the inclusion, but returned to bulk values away from the protein-membrane interface with a decay length $\lambda_D \sim 15$ Å (comparable to the length of a lipid molecule). In their model the protein was assumed to be a cylinder and the slope condition was allowed to relax by using *natural BCs* on the curvature (See S5 for details on boundary conditions). Their model could describe experiments carried out on gramicidin (30) by only modulating the compression modulus as:

$$K_a(x,y) = \left[1 + (\Theta - 1)\cdot \exp\left(-\frac{r - r_0}{\lambda_D}\right)\right] K_{a,B}, \quad \text{for} \quad r \geq r_0, \tag{S25}$$

where $K_{a,B}$ is the bulk compression modulus, $\Theta \sim 4.5$ is the fitted phenomenological hardening factor, r_0 is the protein radius, and r is the radial distance from the protein center. Hence, lipids located $r - r_0 > 15$ Å from the protein have bulk-like behavior. Recently Lee et al. (22) noted that this approach still fails to provide bilayer thickness values consistent with molecular dynamics. We presume that these differences are due to the simplified protein representation in the elastic model and not the theoretical methodology. Therefore, in the main text we have implemented the Kim et al. (1), Partenskii and Jordan (24) hardening effect in the context of specific protein geometry. In our model, the upper (+) and lower (−) leaflet compression moduli follow from Eq. S25:

$$K_a^{\pm}(x,y) = \left[1 + (\Theta^{\pm} - 1)\cdot \exp\left(-\frac{r - r_0^{\pm}}{\lambda_D}\right)\right] K_{a,m}, \quad \text{for} \quad r \geq r_0^{\pm}, \tag{S26}$$

where $K_{a,m}$ is the monolayer bulk compression modulus, which we assume is half of the bilayer value $K_{a,B}$. For non-cylindrical proteins, the quantity $r - r_0^{\pm}$ is computed by identifying the membrane-protein contact point, $r_0^{\pm}$, that lies along the radial line connecting r to the origin. In general, the hardening field will be different in the upper and lower leaflets due to differences in the protein geometry in both leaflets (as in Fig. S5) leading to $K_a^+(x,y) \neq K_a^-(x,y)$. Therefore, when studying the distortions induced by arbitrary shape proteins, the bilayer compression modulus including the effects of hardening is readily given by the effective modulus K_{eff} in expression Eq. S21. Throughout this work, we set $\Theta^{\pm} \sim 4.5$ based on the gramicidin analysis in Ref. (24); however, it is possible to compare our calculations to deformation profiles determined from all-atom simulations to arrive at appropriate hardening values.

S4.5. Gaussian curvature

The Gaussian curvature energy in the upper leaflet is given by (see Refs. (11, 31, 32)):

$$E_G = -\frac{K_G}{2}\int_{\Omega^+} \vec{\nabla}\cdot\left[\left(\vec{\nabla}\vec{n}\right)\vec{n} - \left(\vec{\nabla}\cdot\vec{n}\right)\vec{n}\right] dxdy, \tag{S27}$$

where K_G is the Gaussian bending modulus, $\vec{n} = \nabla h^+$ is the two dimensional surface normal (neglecting the z-component), and we have dropped much of the leaflet specific notation. There is a similar energy term corresponding to the lower leaflet. In the expression above, we have used the notation $\vec{\nabla}\vec{n} = n_{j,k}$ to represent a second order tensor containing the derivatives of the normal vector $\vec{n}$ and hence $\left(\vec{\nabla}\vec{n}\right)\vec{n} = \left(\vec{n}\cdot\vec{\nabla}\right)\vec{n} = n_{j,k}n_k$ is a vector. With the divergence theorem, we can recast the Gaussian bending energy on the boundary $\partial\Omega$ as:

$$E_G = -\frac{K_G}{2}\oint_{\partial\Omega}\left[\left(\vec{\nabla}\vec{n}\right)\vec{n} - \left(\vec{\nabla}\cdot\vec{n}\right)\vec{n}\right]\cdot(-\vec{r})\, dl, \tag{S28}$$

where we define $\vec{r}$ as the outer normal to the surface describing the boundary $\partial\Omega$ in the x-y plane. Next, we show that the Gaussian contribution only depends on the boundary condition $\vec{n} = \vec{n}_0 = \nabla\vec{h}_0$ on $\partial\Omega$ (31, 32). To do this, we first define the tangential surface gradient operator (see Ref. (31)):

$$\vec{\nabla}_T\vec{n} = \vec{\nabla}\vec{n} - \left(\vec{\nabla}\vec{n}\right)\vec{r}\otimes\vec{r}, \tag{S29}$$

which essentially removes any contribution of the tensor $\vec{\nabla}_T\vec{n}$ in the normal direction to the surface $\vec{r}$. Consequently, $\vec{\nabla}_T\vec{n}$ only depends on tangential derivatives, or in other words, only values of $\vec{n} = \vec{n}_0$ on $\partial\Omega$. Making use of $\vec{\nabla}_T\vec{n}$, we can rewrite Eq. S28 as:

$$\begin{aligned}\left[\left(\vec{\nabla}\vec{n}\right)\vec{n} - \left(\vec{\nabla}\cdot\vec{n}\right)\vec{n}\right]\cdot\vec{r} &= n_{i,j}n_j r_i - n_{i,i}n_j r_j \\ &= \left(n_{i,j} - n_{i,k}r_k r_j\right)n_j r_i - \left(n_{i,i} - n_{i,k}r_k r_i\right)n_j r_j \\ &= \left[\left(\vec{\nabla}_T\vec{n}\right)\vec{n} - \mathrm{tr}\left(\vec{\nabla}_T\vec{n}\right)\vec{n}\right]\cdot\vec{r}.\end{aligned} \tag{S30}$$

From Eq. S30, we see that the Gaussian contribution Eq. S28 is only a function of normals $\vec{n}_0$ on the boundary. Consequently, if $\vec{n}_0$ is fixed as part of the boundary conditions, then there is no variation of the Gaussian energy E_G with respect to $\vec{n}$ at the boundary ($\delta(E_G)/\delta\vec{n} = 0$) and there is no contribution of the Gaussian component to the minimization equations. Thus, Eq. S28 does not influence the minimum energy configuration, but it must be included to determine the total energy of the system.

S4.5.1. Gaussian bending modulus K_G

Let c_1 and c_2 be the two principal curvatures such that mean curvature is $2H = c_1 + c_2$ and the Gaussian curvature is $K = c_1 \cdot c_2$. Then the energy density associated with changes in curvature is given by(9):

$$G = \frac{1}{2}K_c(H^2) + K_G(K) = [c_1, c_2]\cdot[\mathbf{A}]\cdot[c_1, c_2]^T, \quad \mathbf{A} = \begin{bmatrix} K_c & K_c + K_G \\ K_c + K_G & K_c \end{bmatrix}, \tag{S31}$$

where K_c is the bending modulus. For the free energy G to have a minimum, the matrix $\mathbf{A}$ must be positive definite, which requires $2K_c > -K_G > 0$. In the main text, we have used $K_G \sim -0.9K_c$ as recently measured from simulation (33).

S5. Boundary conditions at the membrane-protein contact curve

The total energy of the membrane-protein system (G^T) is given by the sum of the membrane elastic energy ($G^{(me)}$), the electrostatic energy ($G^{(e)}$), and the nonpolar energy $G^{(np)}$. For the elastic energy $G^{(me)}$, we assume that the only unknowns are the fields $u^+(x, y)$ and $u^-(x, y)$. The energy minimization is obtained using the variational formulation:

$$\delta G^{(me)}(u^+, u^-) = \delta G^{(me)}_{u^+} + \delta G^{(me)}_{u^-} = 0, \tag{S32}$$

where δG_{u^+} and δG_{u^-} represent the variation in energy resulting from variables u^+ and u^-, respectively. Eq. S32 yields the equilibrium shape equations of the membrane as well as a set of requirements (boundary conditions BCs) that the membrane deformation variables must satisfy at the boundary interface(34).

To see the role and physical significance of the BCs, we write the membrane's elastic energy functional $\delta G^{(me)}$ as the sum of the interior membrane surface contributions ($\delta G^{(me)}_\Omega$) and the contribution at the boundary edge ($\delta G^{(me)}_B$) (34):

$$\delta G^{(me)}\left(u^+, u^-\right) = \delta G^{(me)}_\Omega\left(u^+, u^-\right) + \delta G^{(me)}_B\left(u^+, u^-\right). \tag{S33}$$

Under the assumption that no external forces are acting over the interior surface of the membrane and that the only perturbations are due to the inclusion on the internal edge-boundaries, then the first term $\delta G^{(me)}_\Omega$ over the interior surface yields the Euler-Lagrange equations presented in the main text:

$$\nabla^4 u^+ - \nabla^2 J_0^+ - \gamma\nabla^2 u^+ + \beta\left(u^+ - u^-\right) = 0, \quad \text{in } \Omega_M, \tag{S34}$$

$$\nabla^4 u^- + \nabla^2 J_0^- - \gamma\nabla^2 u^- + \beta\left(u^- - u^+\right) = 0, \quad \text{in } \Omega_M, \tag{S35}$$

$$\nabla^4 u^- + \nabla^2 J_0^- - \gamma\nabla^2 u^- + \frac{\beta}{2}\left(u^- - u_B^+\right) = 0, \quad \text{in } \Omega_1, \tag{S36}$$

$$\nabla^4 u^+ - \nabla^2 J_0^+ - \gamma\nabla^2 u^+ + \frac{\beta}{2}\left(u^+ - u_B^-\right) = 0, \quad \text{in } \Omega_2, \tag{S37}$$

The second term $\delta G_B^{(me)}$ in Eq. S33 must account for the external shearing force $p_{ext}^{\pm}$ and mechanical moments $m_{ext}^{\pm}$ imposed by the inclusion at the edges (interior boundary) of the upper and lower leaflets, respectively. The latter yields the following set of allowable BCs (24):

$$\delta u^+ \left[p^+(u^+,u^-) - p_{ext}^+\right] + \delta\left(\nabla u^+ \cdot \vec{r}_2\right)\left[m^+(u^+,u^-) - m_{ext}^+\right] = 0 \quad \text{at the upper leaflet boundary,} \tag{S38}$$

$$\delta u^- \left[p^-(u^+,u^-) - p_{ext}^-\right] + \delta\left(\nabla u^- \cdot \vec{r}_1\right)\left[m^-(u^+,u^-) - m_{ext}^-\right] = 0 \quad \text{at the lower leaflet boundary,} \tag{S39}$$

where $\vec{r}_1$ is the unit vector pointing perpendicular to the curve described by the lower leaflet-protein interface and $\vec{r}_2$ is the unit vector pointing perpendicular to the curve described by the upper leaflet-protein interface (see Fig. 1 B in the main text). The variable $p^{\pm}$ represents the internal forces and $m^{\pm}$ are the internal moments generated at the interface by the stressed upper and lower leaflets.

From Eq. S38 and Eq. S39, we see that there there are several different BCs that satisfy the physical situation. The first, and most intuitive situation, is *fixed BCs*, where $u^{\pm}$ and $\vec{\nabla}u^{\pm}$ are predetermined at the boundaries. In this case, variations on the deformation variables at the boundary are zero ($\delta u^{\pm} = \delta\nabla u^{\pm} = 0$) and Eq. S38 - Eq. S39 are immediately satisfied. For the protein induced membrane distortion problem, we have following set of *fixed* conditions (See Refs. (24)):

$$\begin{aligned} &u^{\pm} = 0, \quad && \vec{\nabla}u^{\pm} = 0 && \text{far away from inclusion, and} \\ &u^{\pm} = u_B^{\pm}, \quad && \vec{\nabla}u^- \cdot \vec{r}_1 = S^-, \quad \vec{\nabla}u^+ \cdot \vec{r}_2 = S^+ && \text{at the protein-monolayer interface,} \end{aligned} \tag{S40}$$

where $S^{\pm}$ reflects the monolayer slope, or contact angle, at the point of contact with the protein. The fixed conditions *far away from the inclusion* in Eq. S40 are commonly used in the literature since it is expected that the protein induced membrane deformations should decay to bulk values; however, there is more disagreement about the appropriate BCs *at the protein-monolayer interface* in Eq. S40 (22). Earlier work found that setting the slopes equal to zero at the protein-membrane interface yielded compatible energetics with experiments carried out on gramicidin (24, 36, 37). Yet there is no formal justification for the zero slope condition, and more recent comparison with MD simulations suggests that the zero slope boundary condition fails to properly describe membrane deformations near the protein (22).

A second set of BCs compatible with Eq. S38 and Eq. S39 arise from the *physical* constraints of forces and torques at the membrane-protein interface (24):

$$p^+(u^+,u^-) = p_{ext}^+ \quad \text{and} \quad m^+(u^+,u^-) = m_{ext}^+ \quad \text{at the upper leaflet boundary,} \tag{S41}$$

$$p^-(u^+,u^-) = p_{ext}^- \quad \text{and} \quad m^-(u^+,u^-) = m_{ext}^- \quad \text{at the lower leaflet boundary.} \tag{S42}$$

It is not possible to know the analytic form of the constraints $p_{ext}^{\pm}$ and $m_{ext}^{\pm}$, thus precluding an easy implementation of these conditions. However, a special situations, referred to as *natural BCs*, arises when $u^{\pm}$ and/or $S^{\pm}$ are allowed to freely and independently adjust to the effects of the inclusion (22, 24). When $u^{\pm}$ is free to adjust, it implies no external forces are being applied ($p^{\pm} = 0$), while freely adjusting slopes ($S^{\pm}$) imply no externally applied moments ($m^{\pm} = 0$) (24). For instance, instead of fixing the value of $S^{\pm}$ at the boundary, many authors have used the alternative natural BCs of prescribing the *curvature* ($\nabla^2 u^{\pm} = 0$). For the case of gramicidin, it was determined that natural BCs on the curvature poorly correlated with experimental energies (22). Moreover, a formal mathematical derivation shows that the spontaneous J_0 and Gaussian modulus K_G should directly influence the curvature boundary condition (38). Both of these quantities are usually neglected in continuum elastic models that use the natural boundary condition on curvatures (22, 38). This could potentially contribute to the discrepancies reported between continuum elastic predictions and simulation/experiment.

S5.1. What are the correct boundary conditions for real proteins?

The unknown functional form of the forces $p_{ext}^{\pm}$ and torques $m_{ext}^{\pm}$ at the boundary precludes the use of a purely elastic continuum model for the membrane. Instead we use a hybrid continuum-atomistic model that couples the membrane deformation energy ($G^{(me)}$), non-polar energy ($G^{(np)}$) and electrostatic energy ($G^{(e)}$). The set of boundary conditions of the elastic model that minimizes the total energy of the system (G^T) is the key coupling element between the three explicit energies appearing in our hybrid approach. In the main text, we describe the optimization procedure

used to minimize the energy by optimally choosing BCs, and these optimized displacement values at the protein-membrane boundary ($u_B^{\pm}$) are shown in Fig. 3 of the main text.

For completeness, the optimized slope boundary conditions ($S^{\pm}$) together with the slopes extracted from MD are shown in Fig. S6. The MD slope data is rather noisy due to the highly fluctuating nature of the gramicidin protein (center of mass translations, rotations, off axis tilting, and rotamer flipping), but our continuum slope predictions are in good agreement with the *average* values from MD. Convergence of the search over the boundary conditions depends on the protein's geometry and size, but generally it requires 500 to 1500 iterations to achieve an absolute convergence in the energy of 0.5 kcal/mol. Typical optimization times are about 2 to 7 hours on a desktop computer using a single core. As shown in Fig. S6, our optimized slopes are slightly positive and not zero as suggested by previous authors (13, 36, 37). Our solutions show evidence that at the protein-membrane interface, the slopes adapt in order to reduce the elastic penalty. This result agrees with the expected physical behavior for an elastic slab that is compressed. The hydrophobic region of gramicidin is slightly smaller than the hydrophobic thickness of the membrane (POPC), and in order to reduce the compression penalty near the protein the membrane returns to its undeformed shape more quickly resulting in non-zero slope. Having a positive slope will have a favorable effect to reduce compression at the expense of introducing curvature into the system. Including lipid hardening effects near the protein tends to increase the degree of the slope since the compression penalty increases. Despite our finding of a non-zero slope, the values reported here are smaller than the values reported previously (24) when using using lipid hardening in a membrane elastic model together with natural boundary conditions (free slope).

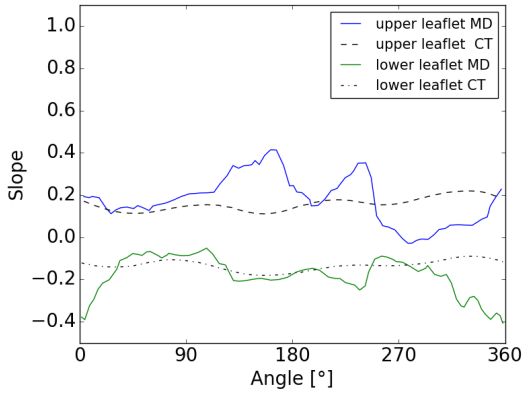

Figure S6: Predicted slopes at the protein-membrane boundary obtained from continuum calculations. The dotted line represents the optimal slope at the upper leaflet, and the dashed line corresponds to the slope values at the lower leaflet. The x-axis is the angular parameterization of the displacement along the membrane-protein boundary.

S6. Convergence of the continuum elastic energy.

We tested the convergence of our numeric solver for three different cases: an idealized cylindrical inclusion with $r_0 = 15$ Å, a configuration of gramicidin A examined in the main text, and the configuration of nhTMEM16 examined in our previous work (10). Each case has its own advantage. The cylinder has an analytic solution that we used to assess the absolute convergence of our method, while the later two cases are real proteins. Gramicidin is small and largely cylindrical, while nhTMEM16 is a large dimer with 20 transmembrane helices total (10). For the cylinder and gramicidin, solutions were calculated on a 100 Å by 100 Å grid, but nhTMEM16 is much larger, it was calculated on a 200 Å by 200 Å grid (10). For each boundary, we applied symmetric displacement boundary conditions: $u_B^{\pm} = \mp 1.5 \pm 1.5 \cdot \mathrm{Sin}(2t) \mp 1.5 \cdot \mathrm{Cos}(t)$. For the cylinder, a slope of zero was applied with no Partenskii-Jordan hardening near the protein, while the other two systems employed a hardening factor of 4.27 and a slope factor of -0.04. The error on the membrane displacement field was evaluated using the L^{∞}-norm, while the relative error was used to assess convergence of the total membrane energy (G^T). Analytic solutions do not exists for the gramicidin and nhTMEM16 cases, so the errors were calculated relative to the solution obtained at the highest grid density. In all

cases, the greatest error over the entire displacement field is less than 0.7 Å when the grid spacing is less than 1.5 Å, which is greater than 64 grid points for A and B and greater than 128 grid points for C (Fig. S7). For the cylindrical inclusion, the error in the L^∞-norm asymptotically approaches 0.065 Å rather than 0 Å. The element corresponding to this maximum error is located on the outer boundary at 50 Å, where we assumed that the displacement field returned to zero in the numeric calculation, but we assume boundaries at infinity in the analytic solution. Thus, the true error in the numeric solver is even smaller than what is presented, due to inconsistencies between our numeric calculation and our analytic reference. The relative energies have converged to approximately 5 % in all cases when the grid spacing is 1 Å (Fig. S7 D-F). For all calculations in the main text, we use a grid spacing of 1 Å.

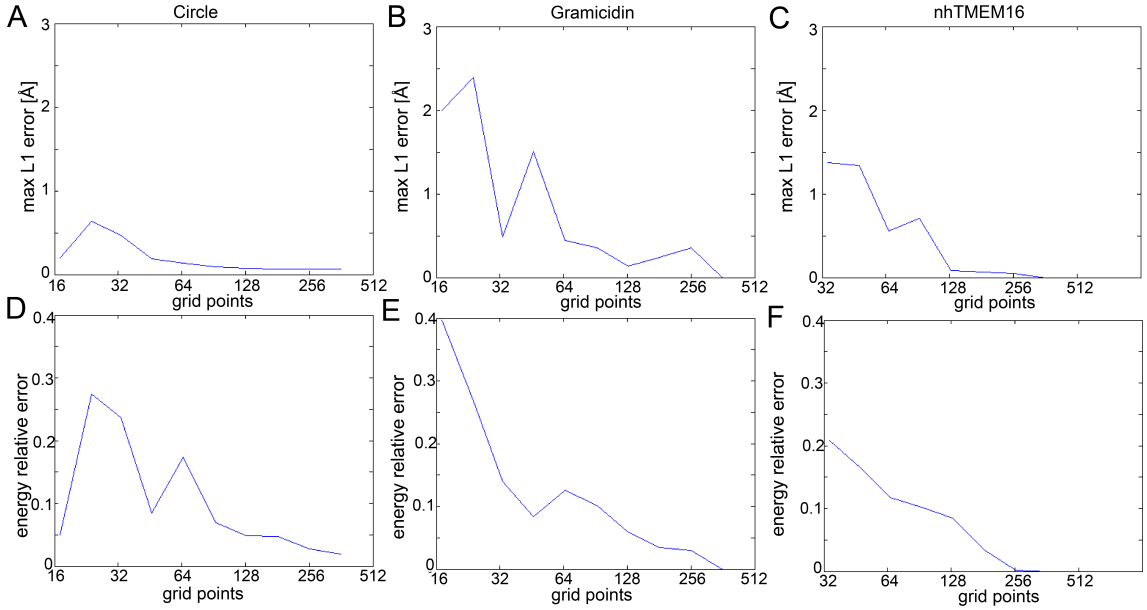

Figure S7: Convergence of membrane distortions on boundaries of different size and complexity. (A-C) L^∞-norm of the membrane shape variable for a cylinder of radius 15 Å, gramicidin, and nhTMEM16, respectively. The error is $E^\infty = \max\{u_{i,j}^{\text{numeric}} - u_{i,j}^{\text{analytic}}\}$ for the cylinder and $E^\infty = \max\{u_{i,j}^{\text{numeric}} - u_{i,j}^{\text{numeric max refinement}}\}$ for the two real proteins, and the indices i, j correspond to all elements in the xy-plane. Note that this error is identical to the maximum component of the L^1-norm as indicated in the figure label. (D-F) Relative error in the elastic energy for the cylinder, gramicidin, and nhTMEM16, respectively. The total energy for each test case was 8.8, 17.9, and 31.5 kcal/mol, respectively, where the last two values were determined from the numeric solution at the highest grid density and the former was determined analytically.

S7. Membrane height profiles from hybrid continuum-atomistic model.

Finally, we wanted to show the full 2D membrane profile predicted from our hybrid-continuum atomistic model (Fig. S8) using the self-consistently optimized membrane boundary displacements (shown in Fig. 4 of the main text) and slopes (Fig. S6). At the outer edges of the solution domain, we have imposed far field boundary conditions ($u^\pm = \nabla u^\pm = 0$). The corresponding membrane shape is quite similar in nature to the profiles from MD shown in Fig. 2A,B (main text); however, they are not identical for several important reasons. First, the MD simulations impose periodic boundaries and the continuum calculation in (Fig. S8) do not. Second, the profiles from the MD simulations are averaged over the entire simulation trajectory, while the continuum boundary conditions were taken from a small subset of protein configurations around the most populated orientation. As discussed throughout the manuscript, it is not advisable to closely compare deformation profiles of averaged membranes with static snapshots.

Supporting References

[1] T Kim, K Lee, P Morris, R W Pastor, O S Andersen, and W Im. Influence of Hydrophobic Mismatch on Structures and Dynamics of Gramicidin A and Lipid Bilayers. *Biophys. J.*, 102(7):1551–1560, 2012.

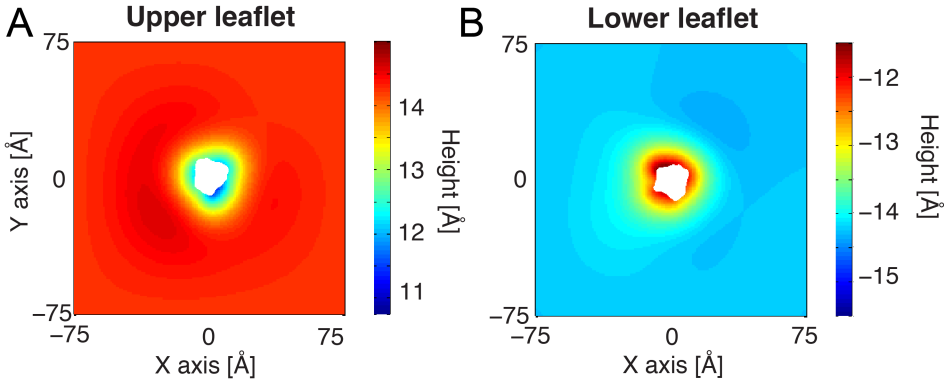

Figure S8: Gramicidin induced membrane deformations in the upper leaflet (A) and lower leaflet (B) calculated using our hybrid-continuum atomistic model. The boundary conditions at the protein-membrane interface are determined by a self-consistent optimization of our hybrid model. At the outer edges of the box we have imposed far field boundary conditions for the membrane deflections $u^{\pm} = \nabla u^{\pm} = 0$.

[2] KA Sharp and B Honig. Electrostatic interactions in macromolecules: Theory and applications. *Annual Review of Biophysics and Biophysical Chemistry*, 19(1):301–332, 1990. doi: 10.1146/annurev.bb.19.060190.001505.

[3] Nathan A Baker, David Sept, Simpson Joseph, Michael J Holst, and J Andrew McCammon. Electrostatics of nanosystems: Application to microtubules and the ribosome. *Proceedings of the National Academy of Sciences*, 98(18):10037–10041, 2001.

[4] K M Callenberg. *Membrane bending is critical for assessing the thermodynamic stability of proteins in the membrane.* PhD thesis, University of Pittsburgh, 2013.

[5] F V Marcoline, N Bethel, C J Guerriero, J L Brodsky, and M Grabe. Membrane protein properties revealed through data-rich electrostatics calculations. *Structure*, 23(8):1526–1537, 2015.

[6] N R Latorraca, K M Callenberg, J P Boyle, and M Grabe. Continuum approaches to understanding ion and peptide interactions with the membrane. *The Journal of Membrane Biology*, 247(5):395–408, 2014. ISSN 0022-2631. doi: 10.1007/s00232-014-9646-z.

[7] Michel F Sanner, Arthur J Olson, and Jean-Claude Spehner. Reduced surface: An efficient way to compute molecular surfaces. *Biopolymers*, 38(3):305–320, 1996.

[8] D Sitkoff, N Ben-Tal, and B Honig. Calculation of alkane to water solvation free energies using continuum solvent models. *The Journal of Physical Chemistry*, 100(7):2744–2752, 1996. doi: 10.1021/jp952986i.

[9] M Deserno. Fluid lipid membranes: From differential geometry to curvature stresses. *Chemistry and Physics of Lipids*, 185(0):11 – 45, 2015. ISSN 0009-3084. doi: http://dx.doi.org/10.1016/j.chemphyslip.2014.05.001.

[10] D Argudo, N P Bethel, F V Marcoline, and M Grabe. Continuum descriptions of membranes and their interaction with proteins: Towards chemically accurate models. *Biochimica et Biophysica Acta (BBA) - Biomembranes*, 1858:1619 – 1634, Jul 2016. ISSN 0005-2736. doi: http://dx.doi.org/10.1016/j.bbamem.2016.02.003.

[11] Max C Watson, Evgeni S Penev, Paul M Welch, and Frank L H Brown. Thermal fluctuations in shape, thickness, and molecular orientation in lipid bilayers. *J. Chem. Phys.*, 135(24):244701, 2011. doi: http://dx.doi.org/10.1063/1.3660673.

[12] J.-B. Fournier. Microscopic membrane elasticity and interactions among membrane inclusions: interplay between the shape, dilation, tilt and tilt-difference modes. *The European Physical Journal B - Condensed Matter and Complex Systems*, 11(2):261–272, 1999. ISSN 1434-6028. doi: 10.1007/BF03219168.

[13] H W Huang. Deformation free energy of bilayer membrane and its effect on gramicidin channel lifetime. *Biophys. J.*, 50(6):1061–1070, 1986.

[14] F Schmid. Are stress-free membranes really ”tensionless”? *EPL*, 95(2):28008–, 2011.

[15] H Diamant. Model-free thermodynamics of fluid vesicles. *Phys. Rev. E.*, 84:061123–, 2011.

[16] Max C Watson, Alex Morriss-Andrews, Paul M Welch, and Frank L H Brown. Thermal fluctuations in shape, thickness, and molecular orientation in lipid bilayers. II. Finite surface tensions. *J. Chem. Phys.*, 139(8):084706, 2013. doi: http://dx.doi.org/10.1063/1.4818530.

[17] A Samuel Safran. *Statistical Thermodynamics of Surfaces, Interfaces, and Membranes*. Westview Press, Boulder, Colorado, 2003. Frontiers in Physics.

[18] A F Bitbol, D Constantin, and J.-B. Fournier. Bilayer Elasticity at the Nanoscale: The Need for New Terms. *PLos ONE.*, 7(11):–, 2012. doi: 10.1371/journal.pone.0048306.

[19] S Choe, K A Hecht, and M Grabe. A continuum method for determining membrane protein insertion energies and the problem of charged residues. *J. Gen. Physiol.*, 131(6):563–573, 2008.

[20] Keith M Callenberg, Om P Choudhary, Gabriel L de Forest, David W Gohara, Nathan A Baker, and Michael Grabe. Apbsmem: A graphical interface for electrostatic calculations at the membrane. *PLoS ONE*, 5(9):e12722–, 09 2010. doi: 10.1371/journal.pone.0012722.

[21] K M Callenberg, N R Latorraca, and M Grabe. Membrane bending is critical for the stability of voltage sensor segments in the membrane. *The Journal of General Physiology*, 140(1):55–68, 2012. doi: 10.1085/jgp.201110766.

[22] K Lee, R W Pastor, O S Andersen, and W Im. Assessing smectic liquid-crystal continuum models for elastic bilayer deformations. *Chemistry and Physics of Lipids*, 169(0):19 – 26, 2013. doi: http://dx.doi.org/10.1016/j.chemphyslip.2013.01.005. Computational approaches to

understanding lipid-protein interactions.
[23] D Boal. *Mechanics of the Cell*. Cambridge University Press, Cambridge, 2nd edition, 2012.
[24] M B Partenskii and P C Jordan. Membrane deformation and the elastic energy of insertion: Perturbation of membrane elastic constants due to peptide insertion. *The Journal of Chemical Physics*, 117(23):10768–10776, 2002. doi: http://dx.doi.org/10.1063/1.1519840.
[25] Aranda-Espinoza, H and Berman, A and Dan, N and Pincus, P and Safran, S. Interaction between inclusions embedded in membranes. *Biophys. J.*, 71(2):648–656, 1996.
[26] Miha Fošnarič, Ale š Iglič, and Sylvio May. Influence of rigid inclusions on the bending elasticity of a lipid membrane. *Phys. Rev. E*, 74(5): 051503–, 2006. doi: 10.1103/PhysRevE.74.051503.
[27] R J Bingham, P D Olmsted, and S W Smye. Undulation instability in a bilayer lipid membrane due to electric field interaction with lipid dipoles. *Phys. Rev. E*, 81(5):051909–, 2010. doi: 10.1103/PhysRevE.81.051909.
[28] A C Haselwandter and R Phillips. Connection between oligomeric state and gating characteristics of mechanosensitive ion channels. *PLoS Comput Biol.*, 9(5):1–13, 2013.
[29] C A Haselwandter and R Phillips. Directional interactions and cooperativity between mechanosensitive membrane proteins. *EPL*, 101(6): 68002–, 2013. doi: 10.1209/0295-5075/101/68002.
[30] M Goulian, O M Mesquita, D K Fygenson, C Nielsen, O S Andersen, and A Libchaber. Gramicidin channel kinetics under tension. *Biophys. J.*, 74(1):328–337, 1998.
[31] Robert Hardt, David Kinderlehrer, and Fang-Hua Lin. Existence and partial regularity of static liquid crystal configurations. *Communications in Mathematical Physics*, 105(4):547–570, 1986.
[32] I W Stewart. *The static and dynamic continuum theory of liquid crystals*. Taylor and Francis, London, UK, 2004.
[33] M Hu, H de Jong, S Marrink, and M Deserno. Gaussian curvature elasticity determined from global shape transformations and local stress distributions: a comparative study using the MARTINI model. *Faraday Discuss.*, 161:365–382, 2013.
[34] O Bolza. *Lectures on the Calculus of Variations*. Dover Publications, New York, 1961.
[36] Nielsen, C and Goulian, M and Andersen, O S. Energetics of inclusion-induced bilayer deformations. *Biophys. J.*, 74(4):1966–83, 1998.
[37] Nielsen, C and Ansersen, O S. Inclusion-induced bilayer deformations: effects of monolayer equilibrium curvature. *Biophys. J.*, 79(5): 2583–2604, 2000.
[38] G Brannigan and F L H Brown. Contributions of Gaussian Curvature and Nonconstant Lipid Volume to Protein Deformation of Lipid Bilayers. *Biophys. J.*, 92(8):864–876, 2007.